

# Motion of a rigid sphere entering and penetrating a deep pool

Prasanna Kumar Billa<sup>1</sup>, Tejaswi Josyula<sup>1,3</sup> and Cameron Tropea<sup>1,2†</sup>,  
Pallab Sinha Mahapatra<sup>1‡</sup>

<sup>1</sup>Department of Mechanical Engineering, Indian Institute of Technology Madras, 600036, India

<sup>2</sup>Institute for Fluid Mechanics and Aerodynamics, Technical University of Darmstadt, 64287, Germany

<sup>3</sup>Current Address: FLOW, Department of Engineering Mechanics, KTH Royal Institute of Technology Stockholm, 11428, Sweden

(Received xx; revised xx; accepted xx)

In this study, we experimentally examine the behavior of a free falling rigid sphere impacting normally onto, and penetrating into a quiescent liquid pool. Parameters, which are varied include the impact velocity, the density, and the diameter of the sphere. Observations of the sphere trajectory in time are made using two orthogonally placed high-speed cameras, yielding the velocity and acceleration vector through repeated differentiation of the time resolved trajectories.

Upon penetration, the sphere goes through three very distinct phases of penetration, denoted as the submersion, deceleration and settling phase, each clearly identifiable through either features seen in trajectory direction or in changes of velocity. These phases exist for all impact Reynolds numbers and density ratios investigated, and their respective duration remain astoundingly constant in terms of dimensionless time. The motion of the sphere is analysed using a scalar force balance for each of instantaneous drag and lift, yielding quantitative estimates of the drag and lift coefficients throughout the trajectory. The variation of these forces can be phenomenologically explained by unsteady wake behavior arising from strong deceleration and through transient asymmetry, leading to variations in trajectory curvature. Despite the large trajectory randomness observed in repetitive experiments, there exist strong commonalities in motion behavior.

**Key words:** drag coefficient, trajectory imaging, unsteady wake, flow past a sphere, force balance on a sphere

## 1. Introduction

Solid bodies impacting and penetrating into a quiescent liquid pool is a widely observed phenomenon with diverse practical applications in ship slamming (Zhao & Faltinsen 1993; Faltinsen 1990), boat hulls (Howison *et al.* 2002), diving (Gregorio *et al.* 2023), bullets (Truscott *et al.* 2014), underwater missiles (May 1975), air-to-sea anti-torpedo defense systems (Von Karman 1929; Richardson 1948; Truscott & Techet 2009), and the transfer of solid objects to the liquid, like releasing oceanographic instruments into the sea (Abraham *et al.* 2014). Water entry problems also have many applications in

† Email address of correspondence: tropea@sla.tu-darmstadt.de

‡ Email address of correspondence: pallab@iitm.ac.in

engineering, sports, and industrial domains, e.g., drag reduction of swimmers, divers and entry and exit of the oars in rowing (Affeld *et al.* 1993). The impact and penetration of solid spheres onto and into a liquid pool, as investigated in the present study, represent a generic simplification of the above mentioned applications.

In some instances, the water entry leads to the formation of a persistent air cavity in the wake of the sphere, depending on the boundary conditions and the wettability of the sphere (Worthington 1883; May 1951; Tan *et al.* 2016; Aristoff & Bush 2009; Aristoff *et al.* 2010; Truscott & Techet 2009; Truscott *et al.* 2012; Mansoor *et al.* 2014; Vakarelski *et al.* 2011; McHale *et al.* 2009; Mansoor *et al.* 2017). It is evident that during the initial stage of impact, with or without an air cavity, the forces acting on the sphere are highly unsteady and that the wake requires a period to become fully developed (Korobkin 1988; Howison *et al.* 1991; Duclaux *et al.* 2007; Aristoff & Bush 2009; Techet & Truscott 2011; Vakarelski *et al.* 2017). What has not been fully elucidated is the necessary time or traversed distance before a flow around the sphere can be considered devoid of entry effects.

The phenomenon of a rigid sphere traversing through a quiescent liquid at Reynolds number ( $Re$ )  $< 1$  (In the present study,  $Re_i$  defined in Table 1 ) was first investigated by Stokes *et al.* (1851), where the viscous forces exerted by the liquid were larger than the inertia of the sphere. For higher impact velocities, the hydrodynamic behavior of various density spheres falling through water has been explored by Kuwabara *et al.* (1983). This study revealed that the spheres exhibited lateral motion away from a pure vertical trajectory. They attribute this to lateral/lift forces exerted on the sphere arising from asymmetric vortex shedding in the wake of the sphere. Taneda (1978) also studied this phenomenon using smoke flow visualization in a wind tunnel and concluded that a side/lift force acts on the sphere due to the asymmetric wake, something that had already been established by Scoggins (1967). These studies confirmed such a side force in the Reynolds number range  $3.8 \times 10^5 < Re < 10^6$ , i.e., above the critical Reynolds number at which laminar-turbulent transition of the boundary layer occurs.

Later, the study of flow visualization of a falling and rising of solid spheres on the quiescent liquid was investigated by Veldhuis *et al.* (2005) using the Schlieren technique for various solid-to-liquid density ratios ranging from 0.5 to 2.63 and various impact  $Re$  ranging from 200 to 4600. This study revealed that the path followed by a sphere changes from a straight vertical line to a deviation in a random direction. This was attributed to the formation of asymmetric vortices in the wake of the sphere. Horowitz & Williamson (2010) conducted an investigation into the behavior of spheres falling freely through a liquid with a relative density  $\rho_s/\rho_l > 1$ , where  $\rho_s$  is the density of the sphere and  $\rho_l$  is the density of the liquid. The study covered a range of Reynolds numbers ( $100 < Re < 15000$ ) and found that the vortex shedding and wake patterns significantly influence the motion of the spheres. Subsequently, Horowitz & Williamson (2010) undertook a comprehensive investigation of vortex formation in the wake of spheres and their dynamics within the liquid, illustrating the wakes and paths of solid spheres using regime maps that delineate distinct motion patterns including vertical, oblique, intermittent oblique, and zigzag trajectories. Ern *et al.* (2011) explored the kinematics and dynamics of spheres moving along irregular paths. The study revealed a close connection between the path instabilities of bluff bodies submerged in viscous liquids and the initiation of instability in the fixed-body wake. The research determined that vortex shedding in the wake plays a crucial role in inducing path instabilities in spheres, causing them to follow irregular trajectories. Truscott *et al.* (2012) conducted a comprehensive study delving into the unsteady forces exerted on spheres of different densities as they impacted a quiescent liquid pool. They successfully developed a technique to estimate hydrodynamic forces

by utilizing both position data and acceleration, which were derived from the trajectory data by fitting of spline curves.

What is not consistently reported in the literature is whether spheres at higher Reynolds numbers exhibit spiraling motion when descending through the liquid. Both Shafir (1965) and Christiansen & Barker (1965) observe corkscrew or spiraling trajectories of the spheres, whereas Kuwabara *et al.* (1983) observe these very seldom. This is insofar an interesting phenomenon since such trajectories infer a sustained lateral/lift force on the sphere, otherwise, the trajectory would transition to a pure vertical settling motion.

The motion of a sphere through a quiescent medium has also been widely studied in relation to sports, whereby roughness and spin can play a decisive role in determining trajectory (Barlow & Domanski 2008; Mehta 2023; Pallis & Mehta 2002). Although neither roughness nor spin is of interest in the present study, certainly the associated interpretation of wake width and wake orientation on drag and lift afforded by these studies are extremely relevant to the present case (Norman & McKeon 2011; Sakib & Smith 2020; Kays *et al.* 1980). Furthermore, because of the strong deceleration of spheres in a liquid medium, the possibility of the Reynolds number decreasing through the critical regime arises. The phenomenon of a critical Reynolds number, at least for a steady flow, has been exhaustively studied, starting with the seminal work of Fage (1936) and now considered textbook material. What arises in the present study is a rapid deceleration of the sphere. Such highly transient flow around a sphere has not been widely studied in the past, although some studies have examined a sphere in an oscillating onflow (Kovaszny *et al.* 1971), albeit using an inviscid assumption to model the measured pressure oscillations on the sphere.

While there is extensive literature on experimental studies, there have also been numerous studies devoted to theoretical and numerical aspects of this problem. By employing the Verlet algorithm, Valladares *et al.* (2003) numerically investigated the motion of a solid sphere traveling through a viscous fluid, and the terminal settling velocities of the spheres were computed for varied viscosity of the fluid and density of the sphere. A complete analytical solution of the sphere falling through the liquid is given by Guo (2011) for various Reynolds numbers for non-zero initial velocities. They have considered a rectilinear fall of a sphere in a quiescent fluid. The Basset–Boussinesq–Oseen (BBO) equation was solved for the acceleration of the sphere inside the viscous liquid. Rubinow & Keller (1961*a*) explored the drag and lift forces experienced by a spinning sphere at low Reynolds numbers ( $Re < 1$ ). Their investigation involved the assumption of a two-dimensional potential flow utilizing the BBO equation. The BBO equation was employed for calculating transverse forces, while a first-order Stokes approximation was utilized to determine the position of the sphere. Using various analytical techniques, Nouri *et al.* (2014) carried out a comprehensive study on the sedimentation of spherical particles in a Newtonian fluid. They presented three simple and exact analytical models for the problem of resolving the nonlinear equation of sedimentation. Lead, copper, and aluminum spheres were used, and the unsteady motion of the sphere was computed using the BBO equation by neglecting the Basset force. When heavy particles like lead, copper, and tungsten fall into a lighter liquid ( $\rho_l \ll \rho_s$ ), the Basset force can be ignored. It was concluded that the analytical and numerical methods can predict the positions, velocities, and accelerations of the particles falling through water.

Despite the numerous previous studies of a sphere moving through a liquid pool, the origin and magnitude of the lateral/lift forces acting on the sphere to divert its trajectory from pure vertical motion have not yet been quantitatively reported. While there is general agreement that unsteady vortex shedding in the wake leads to asymmetric forces,

neither their frequency of occurrence nor their sustainability have been addressed, either phenomenologically or quantitatively. Furthermore, seldom are trajectories followed over a very long time scale, i.e., over a duration in which a steady settling behaviour can be expected. Most previous studies have concentrated on high sphere-to-liquid density ratios ( $> 7$ ), whereby the traversed distance becomes long before settling behaviour occurs, often lying outside the observation field of view. Recognizing these shortcomings, the present study explores a broader range of parameters, including impact Reynolds number and density ratio. Two synchronised cameras are placed orthogonally to each other, for observation of the sphere trajectory in time. Working in a natural coordinate system, the BBO equation is then used to quantitatively estimate the instantaneous drag and lift forces (as dimensionless coefficients) acting on the sphere during its penetration trajectory.

## 2. Experimental setup and methodology

### 2.1. Experimental setup

The experimental setup consists of a clear, translucent acrylic container, high-speed monochrome camera(s), and a vacuum system used to release the spheres. To ensure minimal impact of the walls of the container on the trajectory and underwater behavior of the sphere, the cross-section of the container is large -  $200 \times 200 \text{ mm}^2$ , which is 20 times larger than the diameter of the largest sphere utilized in the present study. The depth of the container is 400 mm. A vacuum system aids the release of spheres from a particular height. By creating a suction pressure at the end of a needle tip, the spheres are firmly held and are released by interrupting this suction pressure. The free falling sphere impacts the liquid with no rotation, as confirmed by the images captured prior to sphere impact. All the experiments are performed in a closed room with an ambient temperature of  $25^\circ\text{C}$ .

Preliminary experiments were conducted by using a single camera (Phantom VEO E-340-L with a Nikon microlens 28 mm, spatial resolution of  $192 \mu\text{m}/\text{pixel}$ ) on one side of the container and backlighting, consisting of a 30W monochromatic light source and a diffuser. From these experiments, it was observed that the spheres exhibited a strong trajectory deviation in the  $x$ - $y$  plane away from the vertical. Therefore, to capture the complete three-dimensional trajectory in time, a second camera was employed. The second high-speed camera (Phantom VEO E-340-L with a Nikon micro lens of focal length 24-85 mm, spatial resolution of  $199 \mu\text{m}/\text{pixel}$ ) was placed orthogonal to and was synchronised with the first camera. The cameras record the sphere motion at 1000 fps, with a resolution of  $1152 \times 1100$  pixels ( $100 \text{ mm} \times 160 \text{ mm}$  in the object plane) and an exposure time of  $400 \mu\text{s}$ . The exposure time leads to a maximum relative motion blur of 28% of the sphere diameter for the smallest sphere (4 mm) with the highest impact velocity (2.8 m/s). However, the motion blur for the 10 mm sphere is only 11% upon impact, and for all spheres, this motion blur decreases rapidly after impact since the velocity immediately goes through a strong deceleration phase. Furthermore, the edge detection routine remains the same at all time steps, so the error through motion blur for the relative motion is neglected. The data is collected while the sphere descends until it traverses out of the field of view of either of the cameras. A pictorial view of the experimental setup is shown in Figure 1a. Figure 1b shows a sample trajectory of a 10 mm sphere with density ratio of 2.16 as observed with the two cameras.

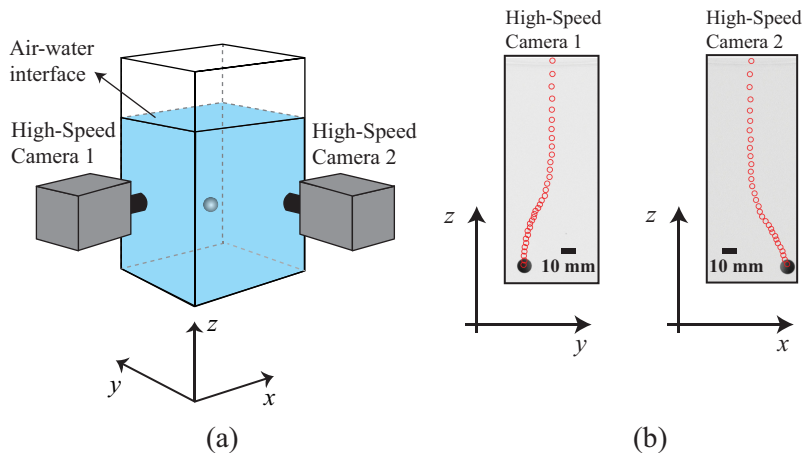


Figure 1: (color online) Two orthogonally and synchronized cameras to record the motion of a rigid sphere after impacting the air-water interface. (a) illustrates schematically the experimental arrangement and the coordinate system used for the image data; (b) a sample trajectory of a sphere with a density ratio of 2.16 and diameter 10 mm is viewed by the two cameras in the  $z$ - $y$  and  $z$ - $x$  planes. The red dots signify the sphere position at equal time intervals of 7 ms.

Table 1: Definitions and range of parameters

Parameter	Symbol	Definition	Range of values
Sphere diameter	$D$	-	4, 6, 10 mm
Density ratio	$\rho^*$	$\rho_s/\rho_l$	2.16, 3.26, 6.08, 7.92
Impact velocity	$v_i$	$\sqrt{2gh}$	1.40, 1.98, 2.80 m/s
Impact Reynolds number	$Re_i$	$v_i D/\nu$	6300 - 31500

## 2.2. Methodology

Table 1 provides the parameters and dimensionless quantities pertinent to this study. The diameter ( $D$ ) of the spheres is measured using a Vernier caliper and their mass ( $m$ ) is determined using an electronic weight balance (Ohaus), yielding their density  $\rho_s$ . The impact velocity ( $v_i \approx \sqrt{2gh}$ ) is derived from the initial release height ( $h$ ) of the sphere, measured from its center to the air-water interface. The Reynolds number ( $Re_i = v_i D/\nu$ ) upon impact ranges from 6300 to 31500.

For these definitions,  $\nu$  is the kinematic viscosity (0.89 mm<sup>2</sup>/s) of the fluid and  $g$  is gravitational acceleration. Throughout the following discussion, length scales are rendered dimensionless using the sphere diameter  $D$ , velocities with the impact velocity  $v_i$ , and time scales using  $D/v_i$ . Dimensionless quantities are designated with the superscript ‘\*’, and unit vectors are written in boldface font. Note that in a similar study, Truscott *et al.* (2012) made time dimensionless with the time to deep seal, i.e., the time at entry air cavity collapse and pinch-off using hydrophobic spheres. They used the same

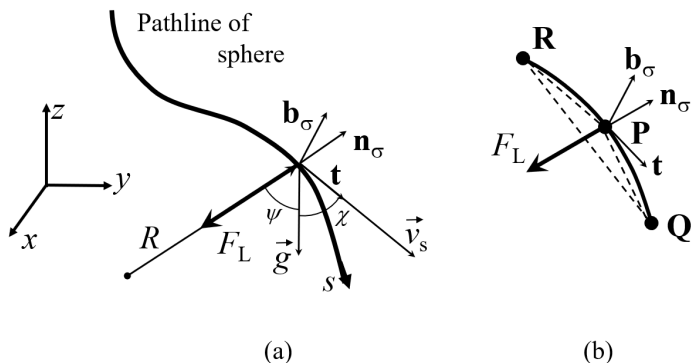


Figure 2: (a) Definition of natural coordinate system based on the sphere pathline. (b) Definition of the plane of curvature and the total lift magnitude  $F_L$ .

reference time for hydrophilic spheres, although no entry cavity formed. In the present experiments with hydrophilic spheres, an air cavity was also not observed; hence, the different normalizing time.

For the presentation of results and the subsequent analysis invoking a force model, it is convenient to work in a natural coordinate system, i.e., in a coordinate system in which the unit vectors of the accompanying triad of the pathline are used as basis vectors. This coordinate system is pictured in Fig. 2a. The unit vector tangential to the pathline is given as

$$\mathbf{t} = \frac{\vec{v}_s}{|\vec{v}_s|} \quad (2.1)$$

where  $\vec{v}_s$  is the velocity vector of the sphere along the pathline  $s$ .  $\sigma$  is the coordinate in the direction  $\mathbf{t}$ ,  $n$  is the coordinate in the direction of the principal normal vector  $\mathbf{n}_\sigma = R d\mathbf{t}/d\sigma$ , and  $b$  the coordinate in the direction of the binormal unit vector  $\mathbf{b}_\sigma = \mathbf{t} \times \mathbf{n}_\sigma$ .  $R$  is the radius of curvature of the pathline in the plane spanned by the normal vectors  $\mathbf{t}$  and  $\mathbf{n}_\sigma$ . The velocity vector  $\vec{v}_s$  is understood to represent the slip velocity, since the pool is quiescent upon sphere impact.

### 2.3. Image Processing

The video images are processed using ImageJ software to subtract the background and to create a binarized image of the sphere inside the liquid. Subsequently, an in-house Matlab<sup>®</sup> code is employed to determine the position of the sphere. The detection of the bottom most point of the sphere is accomplished by utilizing an edge detection technique. The air-water interface is established as the reference point for spatial coordinates ( $z = 0$ ). Similarly, the time instant a sphere makes first contact with the air-water surface is established as the reference point for time ( $t = 0$ ). This time is taken as the first frame in which contact with the liquid has been made.

The accumulated dimensionless path length that the sphere covers is denoted  $s^* = s/D$ , whereby  $s = 0$  is at the air-water interface. The dimensionless lateral displacement at each time step is expressed as  $\delta^* = \sqrt{x^2 + y^2}/D$  (denoted as  $r$  in Truscott *et al.* (2012)). The displacement data is smoothed using an in-house MATLAB function 'loess', a method that involves using linear regression in a locally weighted scatter plot. Subsequently, velocity magnitude  $|\vec{v}_s|$  is computed by differentiating the smoothed displacement data after first fitting that data with a quintic spline function. The dimensionless velocity magnitude is given as  $v_s^* = |\vec{v}_s|/v_i$ . Acceleration data was obtained using a differentiation

of the smoothed velocity data. Time is made dimensionless using the diameter of the sphere and the impact velocity, i.e.,  $t^* = tv_i/D$ .

Given the  $x$ ,  $y$  and  $z$  coordinates of the sphere as a function of time, the curvature of the pathline can be computed as

$$\kappa = \frac{1}{R} = \frac{\sqrt{(z''y' - y''z')^2 + (x''z' - z''x')^2 + (y''x' - x''y')^2}}{(x'^2 + y'^2 + z'^2)^{3/2}} \quad (2.2)$$

where the primes indicate first and second differentiation with respect to time. These differentials are computed numerically using second-order central differences. The angular frequency along the curved pathline is then given as  $\omega = |\vec{v}_s|/R$ , which is a necessary quantity in computing the centrifugal force acting on the sphere, which will be related to the lift force, examined in the following section.

#### 2.4. Force model

In formulating the equations of motion for the sphere, the BBO equation (Zhu & Fan 1998) is used, which includes body forces ( $F_G$  - weight,  $F_B$  - buoyancy), apparent forces ( $F_H$  - Basset or history term,  $F_A$  - added mass), hydrodynamic forces ( $F_D$  - viscous and pressure forces combined as drag) and inertial forces ( $F_I$ ). We will neglect the Saffman lift force (Saffman 1965), applicable only in sheared flow, and any rotational-lift force (Rubinow & Keller 1961*b*), applicable only with rotation/spin of the sphere.

The momentum equation expressed along the direction of motion/pathline can be written as (Crowe *et al.* 2011)

$$\underbrace{\frac{1}{6}\rho_s\pi D^3 \frac{dv_s}{dt}}_{\text{Inertial force}} = \underbrace{\frac{1}{6}\pi D^3(\rho_s - \rho_l)g \cos \chi}_{\text{Body forces}} - \underbrace{\frac{1}{8}C_D\rho_l\pi D^2 v_s^2}_{\text{Drag force}} - \underbrace{\frac{1}{6}C_A\rho_l\pi D^3 \frac{dv_s}{dt}}_{\text{Added mass}} - \underbrace{\frac{3}{2}D^2\sqrt{\pi\mu\rho_l} \int_0^t \frac{1}{\sqrt{t-\zeta}} \frac{dv_s}{dt} d\zeta}_{\text{Boussinesq-Basset term}} \quad (2.3)$$

where  $\zeta = \frac{1}{\sqrt{t}}$  is kernel time of the history term,  $C_D$  is the coefficient of drag, and  $C_A$  is the coefficient of the added mass force. Note that no hydrodynamic lift force has been included in Eq. (2.3). This force will be introduced and discussed below.

The added mass coefficient  $C_A$  is usually taken as 0.5 (Guo 2011) and expresses the kinetic energy imparted into the surrounding fluid through acceleration/deceleration of the sphere. The Boussinesq-Basset term captures the viscous force change due to boundary layer development on an accelerating or decelerating submerged body. These viscous forces are not expected to be significant relative to the inertial and pressure forces involved over large portions of the trajectory; hence, the Boussinesq-Basset term will be neglected in the following analysis (Nouri *et al.* 2014). This is not to say that the transient boundary layer development does not play a central role in determining the trajectory and speed of the sphere, but it is expected to be more through the separation and wake behaviour due to the state of the boundary layer; hence, through the resulting pressure distribution around the sphere. These forces would make themselves apparent in the above equation as variations in the drag force.

The impact Reynolds numbers encountered in this study all lie below approx.  $3 \times 10^4$  and throughout most of the sphere trajectory the values are much lower. For very similar Reynolds numbers Truscott *et al.* (2012) used a drag coefficient of 0.5. They viewed the unsteady added mass as part of the pressure force acting on the sphere, i.e., in the

net hydrodynamic force. In the present study, the experimental data allows all of the remaining terms in Eq. (2.3) to be evaluated; thus, the value of  $C_D$  can and will be computed at each time step.

The terminal velocity of a sphere can be determined by establishing an equilibrium in which the net force acting on the sphere is reduced to zero. The expression for the dimensionless terminal velocity ( $v_t^*$ ) can be obtained by equating the buoyancy force with the drag force plus the weight:

$$v_t^* = \frac{1}{v_i} \sqrt{\frac{4(\rho^* - 1)gD}{3C_D}} \quad (2.4)$$

In this equation a drag coefficient must be prescribed and a value of  $C_D = 0.5$  has been used, assuming at this stage steady flow.

If the pathline has a non-zero curvature ( $\kappa$ ), this implies a force ( $\vec{F}_L$ ) acting in the  $-\mathbf{n}_\sigma$  direction, i.e., perpendicular to  $\mathbf{b}_\sigma$ , as depicted in Fig. 2(b). Since lift force is defined as the force acting perpendicular to the direction of motion (on-flow), the total lift force magnitude,  $\|\vec{F}_L\| = F_L$ , can be computed as the sum of the buoyancy ( $F_B$ ), gravity ( $F_G$ ), and the hydrodynamic (lift) force ( $F_{HL}$ ) acting in the  $-\mathbf{n}_\sigma$  direction. Thus, to compute only the hydrodynamic lift force from the sphere trajectory, the direction of the unit normal  $\mathbf{n}_\sigma$  must be determined. Recognizing that  $\mathbf{n}_\sigma = \mathbf{b}_\sigma \times \mathbf{t}$ , it is necessary to first compute the unit normal  $\mathbf{b}_\sigma$  from the trajectory data. This is done using three points along the trajectory, pictured in Fig. 2(b) as points  $\mathbf{PQR}$ , whereby point  $\mathbf{P}$  is the position of the local force estimate. Point  $\mathbf{R}$  represents the position just before point  $\mathbf{P}$ , and point  $\mathbf{Q}$  is the position following point  $\mathbf{P}$  along the trajectory. The vector  $\overrightarrow{\mathbf{PQ}}$  is derived by computing the forward difference between the coordinates of point  $\mathbf{P}$  and point  $\mathbf{Q}$ . Similarly, the vector  $\overrightarrow{\mathbf{PR}}$  is determined from the points  $\mathbf{P}$  and  $\mathbf{R}$ . This procedure is applied along the trajectory of the sphere from the air-water interface.

Knowing the  $x, y, z$  coordinates of the points  $\mathbf{P}$ ,  $\mathbf{Q}$  and  $\mathbf{R}$ , the unit normal to the subscribed triangle is given by  $\mathbf{b}_\sigma = \overrightarrow{\mathbf{PR}} \times \overrightarrow{\mathbf{PQ}} / \|\overrightarrow{\mathbf{PR}} \times \overrightarrow{\mathbf{PQ}}\|$ . The trajectory unit normal  $\mathbf{t}$ , can be computed using forward differencing around point  $\mathbf{P}$  allowing  $-\mathbf{n}_\sigma = -\mathbf{b}_\sigma \times \mathbf{t}$  to be computed. The angle  $\psi$  is the angle between  $-\mathbf{n}_\sigma$  and the direction of gravity (see Fig. 2(a)). Only the components of buoyancy and gravity along the direction  $-\mathbf{n}_\sigma$  contribute to the total lift, which itself must be equal to the centripetal force; hence,  $(F_G - F_B) \cos \psi + F_{HL} = F_L = m\omega^2 R$  and with the angular frequency given by  $\omega = |\vec{v}_s|/R$

$$(F_G - F_B) \cos \psi + F_{HL} = \frac{m|\vec{v}_s|^2}{R} \quad (2.5)$$

Note that this equation is a scalar equation, since through the  $\cos \psi$  factor, the gravitational and buoyancy forces have been projected onto the  $-\mathbf{n}_\sigma$  vector. Moreover, although the total lift force defined in this manner will always be positive and directed towards the origin of the local curvature radius, as shown in Fig. 2(b), the hydrodynamic lift force could become negative. A negative hydrodynamic lift force would act to reduce the local curvature of the sphere trajectory, i.e., straighten the trajectory. If now the buoyancy and gravity forces are known, then the hydrodynamic portion of the lift force  $F_{HL}$  can be computed and plotted as a function of time or displacement of the sphere. The hydrodynamic lift force is made dimensionless in the form of a lift coefficient,  $C_L$ ,

$$C_L = \frac{F_{HL}}{\frac{1}{2}\rho_l|\vec{v}_s|^2 A} \quad (2.6)$$

where  $A$  is the projected area in the direction of motion, in this case  $\pi D^2/4$ .



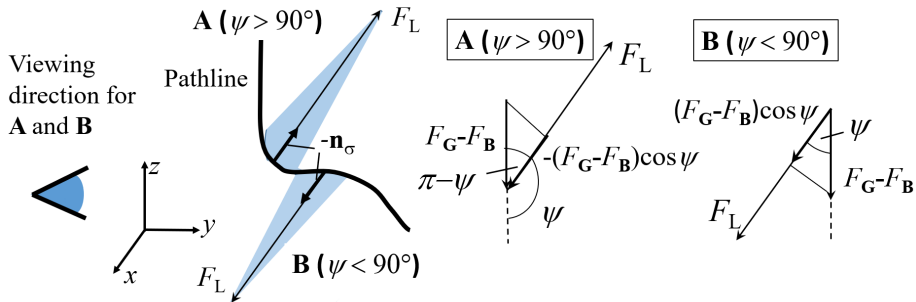


Figure 3: (color online) Graphical representation of example lift force decomposition for two curvatures **A** ( $\psi > \pi/2$ ) and **B** ( $\psi < \pi/2$ ) on opposite sides of an inflection point of the sphere pathline.

In anticipation of properly interpreting the measurement results, the decomposition of the total lift force into body forces and a hydrodynamic lift force is graphically represented in Fig. 3. A pathline is shown which begins vertical downward, exhibits a curvature with  $\psi > \pi/2$ , and then changes curvature orientation. If this curvature change constitutes an inflection point when projected onto any vertical plane, then this leads to a jump of the  $\mathbf{n}_\sigma$  vector by up to  $-\pi$ , in Fig. 3 to  $\psi < \pi/2$ .

Before presenting the results of the experiments, the origin of a lift force arising from an asymmetric wake and the interrelation between drag and lift from such wakes will be phenomenologically discussed. The impact Reynolds number lies in the approximate range  $6300 < Re_i < 31500$ ; however, the sphere decelerates during its trajectory to values of approximately 10% of the impact velocity, thus, the total encountered Reynolds number range is approximately  $630 < Re_i < 31500$ . This range lies in the Newton regime of drag coefficient, in which  $C_D$  takes an almost constant value over all Reynolds numbers and which is significantly below transitional Reynolds numbers for even roughened spheres. On the other hand, the data on which this statement is based comes from experiments in which the on-flow is steady, i.e., no acceleration or deceleration. Thus, accepted drag coefficients for steady flow may not necessarily be applicable over the entire sphere trajectories of the present experiments.

Although the flow and wake may be statistically symmetric around the sphere in this Reynolds number range, the instantaneous wake can be highly asymmetric. Although the time averaged lift coefficients in this Reynolds number range are found to be zero, instantaneous fluctuations have been demonstrated through numerical simulations (Yun *et al.* 2006; Constantinescu & Squires 2004). The transition of the separated boundary layer can be irregular, causing it to temporarily reattach to the surface of the sphere and separate further downstream (Hadžić *et al.* 2002). Both Taneda (1978) and Hadžić *et al.* (2002) observe a progressive wave motion around the sphere for  $10^4 < Re < 3.8 \times 10^5$  by which the separation points rotate around the sphere randomly. Achenbach (1974) also observed this for a very similar Reynolds number range. The drag arises through integration of the pressure around the sphere and is thus highly correlated with the location of flow separation around the sphere: a fluctuating separation will yield a fluctuating drag force. An asymmetric separation and vortex shedding will not only influence the drag, but the asymmetry will also mean that the resultant force will no longer be aligned with the flow direction. Hence, this force will have both drag and lift components. For a free moving body this will result in a change of trajectory, resulting in a new direction of onflow; hence, a new directional orientation of the drag and lift forces.

In summarizing our force model cast in the natural coordinate system, all changes of motion speed of the sphere are attributed to a change in drag plus the body forces along the direction of motion. All changes of direction are attributed to a hydrodynamic lift force plus the body forces acting in the direction of local pathline curvature.

### 3. Measurement Results

#### 3.1. Kinematics of sphere motion

Before discussing the results of the parametric variations conducted in this study, a sample set of data will be examined to illustrate the kinematics of the sphere motion, as shown in Fig. 4. This figure shows a three-dimensional rendition of the trajectory (see Fig. 4a), dimensionless pathline distance ( $s^*$ ) (Fig. 4b), the dimensionless instantaneous velocity magnitude ( $v_s^*$ ) (Fig. 4c), and the dimensionless lateral deviation  $\delta^*$  (Fig. 4d) for a 10 mm sphere ( $\rho^* = 2.16$ ) impacting the pool with a Reynolds number of 31500. The dimensionless velocity magnitude ( $v_s^*$ ) of the sphere in a three-dimensional rendition is depicted using a color bar in Fig. 4a. Two dashed lines have been added to graphs (b)-(d), the first denoting the dimensionless time at which the sphere first deviates more than 10% of its diameter from the vertical trajectory ( $\delta^* > 0.1$ ), and the second denoting the time at which the sphere attains a minimum dimensionless velocity ( $v_s^*$ ). These timelines divide the total time-span into three phases, designated here as

- **Submersion phase**, exhibiting a vertical trajectory and extending up to the time at which the lateral displacement remains below 10% of the maximum diameter of the sphere utilized in the present study.
- **Deceleration phase**, during which the sphere velocity decreases to a minimum value. Note that the sphere is also strongly decelerating in the Submersion phase; however, in this second phase, the sphere completes its deceleration to a minimum velocity.
- **Settling phase**, the remaining time during which the sphere velocity tends towards the nominal terminal velocity in the vertical direction

The end of the deceleration phase coincides exactly with the time at which the lateral deviation of the pathline ( $\delta^*$ ) begins to exhibit strong variations among repetitions of the same experiment. This latter behavior is illustrated in Fig. 5, in which typical lateral deviation curves are shown for repeated experiments using the 10 mm, 6 mm, and 4 mm diameter spheres with  $\rho^* = 2.16$ . Any changes in  $\delta^*$  must necessarily be associated with a lift force, as discussed above. From the Figs. 5a-c, it is evident that the variations in  $\delta^*$  not only depend on the  $Re_i$ , but also on the diameter of the sphere. The influence of the lift force on the magnitude of  $\delta^*$  is expected to be more pronounced for spheres with a smaller diameter and lower  $Re_i$  (as shown in Fig. 5c).

Note that a pure settling velocity in the vertical direction would result in a constant value of  $\delta^*$ .

The behavior of  $\delta^*$  is further elucidated in Fig. 6, in which sample dimensionless lateral deviations are plotted according to the corresponding dimensionless depth  $z^*$  for several density ratios  $\rho^*$ . As expected, with increasing density ratio the period of strictly vertical motion after impact is prolonged and the dimensionless maximum magnitude of  $\delta^*$  is less. This is consistent with the higher inertial and gravitational forces acting on the heavier spheres. What is evident from this data is that only a few of the spheres reach a pure settling trajectory over the period of observation. Hereby, note that the  $z^*$  axis is different

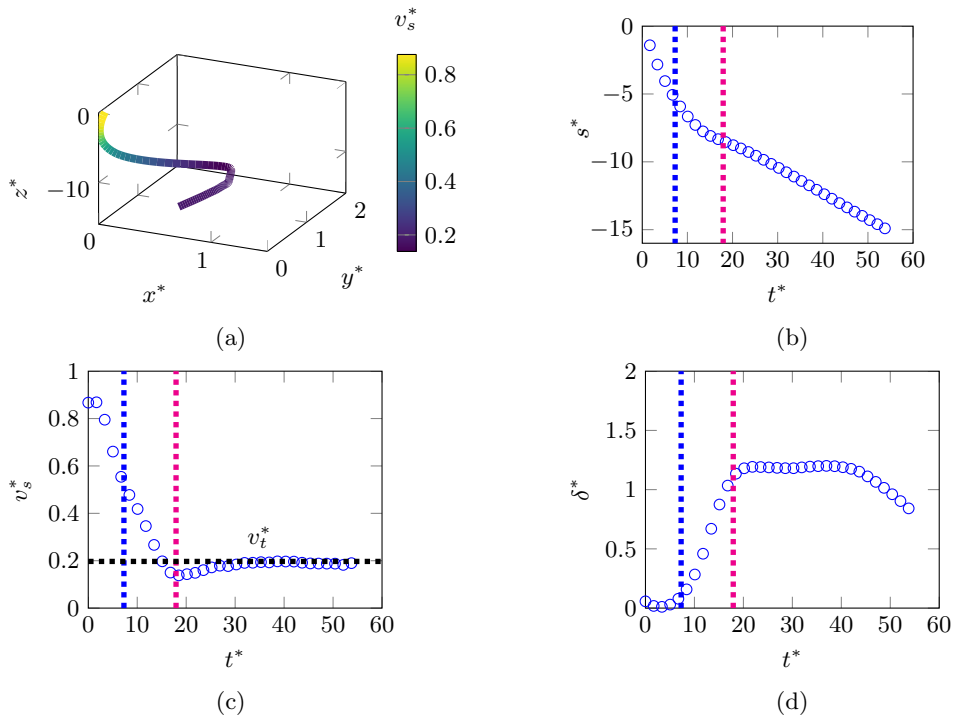


Figure 4: (color online) Motion kinematics of a 10 mm sphere ( $\rho^* = 2.16$ ) entering the pool with an impact Reynolds number of 31500. (a) visualization of three-dimensional trajectory; (b) dimensionless pathline distance over dimensionless time; (c) instantaneous dimensionless velocity over dimensionless time; (d) dimensionless lateral deviation over dimensionless time. The horizontal dashed line in this graph represents the terminal velocity computed according to Eq. (2.4). The dimensionless velocity ( $v_s^*$ ) of the sphere is represented by the colour bar in (a). Data points are spaced equally in time at 6 ms.

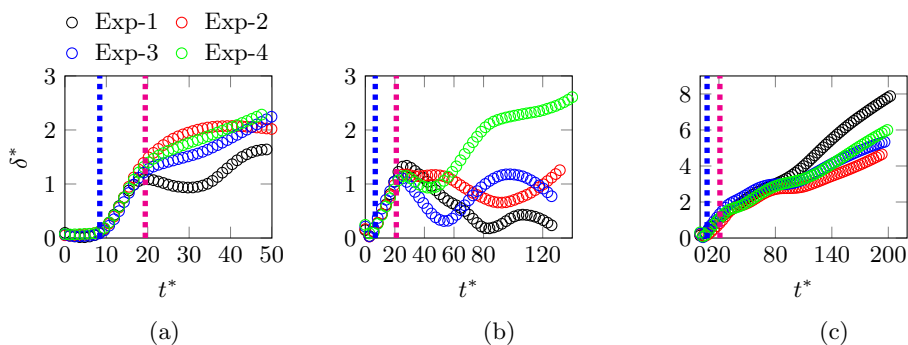


Figure 5: (color online) Examples of measured dimensionless lateral deviations when repeating an experiment: (a) 10 mm sphere at  $Re_i = 22300$ ; (b) 6 mm sphere at  $Re_i = 18900$ ; (c) 4 mm sphere at  $Re_i = 8900$ . All spheres have  $\rho^* = 2.16$ . The time step between the two successive points is 6 ms.

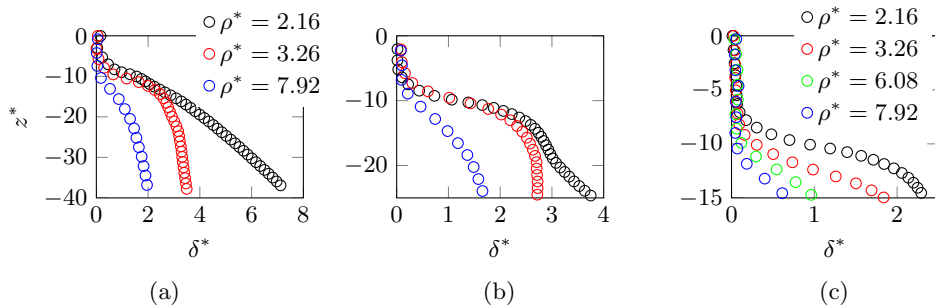


Figure 6: Sample dimensionless lateral deviation ( $\delta^*$ ) against corresponding dimensionless depth ( $z^*$ ) for spheres of various density ratios. (a) 4 mm sphere at  $Re_i = 6300$ ; (b) 6 mm sphere at  $Re_i = 9400$ ; (c) 10 mm sphere at  $Re_i = 15700$ . The time step between trajectory points is 10 ms.

for each graph, i.e., the absolute observation depth plotted for the 4 mm sphere (Fig. 6a) is much larger compared to the 6 mm (Fig. 6b) and 10 mm (Fig. 6c) spheres.

Another observation arising from Fig. 6 is that all spheres exhibit trajectories for which  $\delta^*$  is changing, often at a constant rate (constant slope in the graphs) and often over longer periods of motion. Given that the net difference between buoyancy and gravity forces would act to make the sphere motion vertical, i.e., constant  $\delta^*$ , the conclusion is drawn that during these periods of changing  $\delta^*$ , a sustained hydrodynamic lift force must be acting, counteracting the body forces. The origins of this lift force will be discussed in the following section.

The dimensionless time boundaries between the three phases of motion – submersion, deceleration, settling – are remarkably constant over impact Reynolds number, sphere diameter and density ratio, as shown in Fig. 7 for the dimensionless time at which the submersion phase and deceleration phase ends. Truscott *et al.* (2012) also measured the penetration trajectory of hydrophilic spheres with various density ratios, all impacting with the same Reynolds number ( $U = 3.43$  m/s,  $D = 2.54$  cm). They observed lateral deviations consistently at dimensionless depths of  $z/D \approx 5$ . Converting this dimensionless depth into our dimensionless time  $t^*$  requires the frame rate of their camera, which was not unambiguously given for the data shown in their Fig. 5; however, assuming a frame rate of 840 f.p.s (instead of 1000 f.p.s) yields a very consistent lateral deviation at  $t^* \approx 9.7 - 11.4$ , in excellent agreement with the end of the submersion phase shown in Fig. 7. Only one sphere trajectory in the work of Truscott *et al.* (2012) reached a clear termination of the deceleration phase (minimum velocity in their Fig. 6(b)), and this occurred a dimensionless time of  $t^* = 18$ , also in good agreement with our observations.

### 3.2. Dynamics of sphere motion

In discussing the dynamics of sphere motion, we again begin by examining an example set of data, in this case pertaining to the 10 mm sphere impacting at a Reynolds number of 22300, and shown in Fig. 8. In this figure and in subsequent figures, for clarity, the graphs are plotted only with lines and no symbols. For each of the experimental conditions, a further three sets of data are available and documented in Billa *et al.* (2024). Although there exists a high degree of randomness in the actual trajectories for each experimental repetition, there are also strong commonalities, which will now be discussed in terms of the three phases, beginning with the submersion phase.

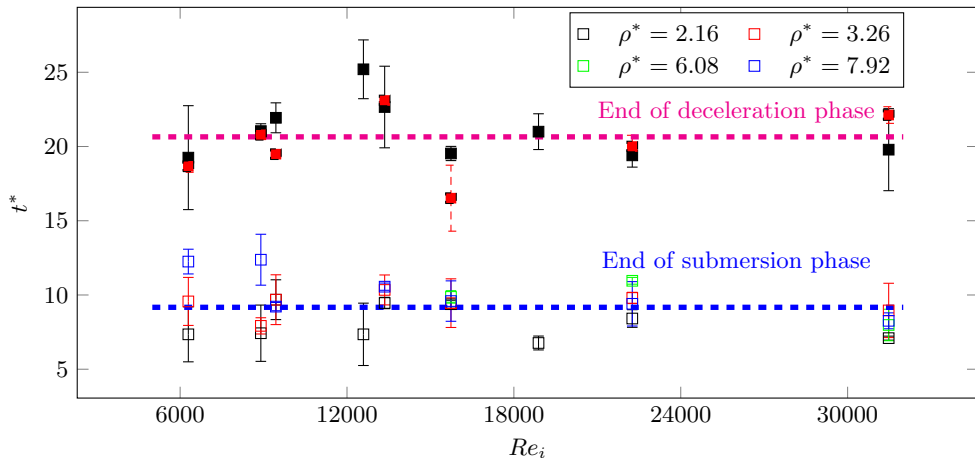


Figure 7: Dimensionless time denoting end of submersion phase and end of deceleration phase of sphere motion as a function of Reynolds number and density ratio. The error bars express one standard deviation computed from four repetitions of the same experiment. For densities  $\rho^* = 6.08$  and  $7.92$  of the 10 mm sphere, the termination of the deceleration phase is not captured, due to the sphere moving beyond the field of view. For the density ratio  $7.92$ , the termination of the deceleration phase for the 4 mm and 6 mm sphere was also not clear, since the velocity did not exhibit a distinct minimum.

#### *Submersion phase*

In the submersion phase, the drag coefficient begins at zero, corresponding to the first contact of the lower sphere surface with the pool free surface. As the sphere submerges into the pool, the drag coefficient increases over the time it takes the sphere to submerge approximately 4-5 diameters. This is only approximate since the velocity is decelerating sharply over this period and  $t^*$  is made dimensionless with the impact velocity. At this time, the drag coefficient reaches a value typical for steady-state flow, i.e.,  $C_D \approx 0.5$ , and retains approximately this value until the end of the submersion phase. Interestingly, and referring back to Fig. 7, this value of  $t^* \approx 4-5$  is virtually constant for all density ratios and Reynolds numbers, whereby Reynolds number has been varied through both impact velocity and sphere diameter. It appears, therefore, that upon entry, the boundary layer on the sphere requires a translation of about 4-5 diameters to become fully developed to a stage devoid of water entry effects.

In the submersion phase, the lift coefficient also begins at zero, corresponding to the pure vertical trajectory with little curvature, and remains low throughout the submersion phase. The angles  $\psi$  and  $\chi$  both exhibit values which remain approximately constant throughout this phase.

#### *Deceleration phase*

We now move to the deceleration phase, marked by the first deviations from the initial vertical trajectory (see Figs. 8a and 8b). The trajectory exhibits strong curvature, which is mirrored in the rapidly changing angles  $\psi$  (Fig. 8e) and  $\chi$  (Fig. 8f), evidently a result of a rapid increase in both drag and lift. Since the first trajectory curvature arises from the vertical state, the lift at this stage can only be attributed to hydrodynamic lift, since the body forces are acting vertical; hence, they are not contributing to the lift force. The large values of drag and lift in this phase are clearly related to asymmetric wake

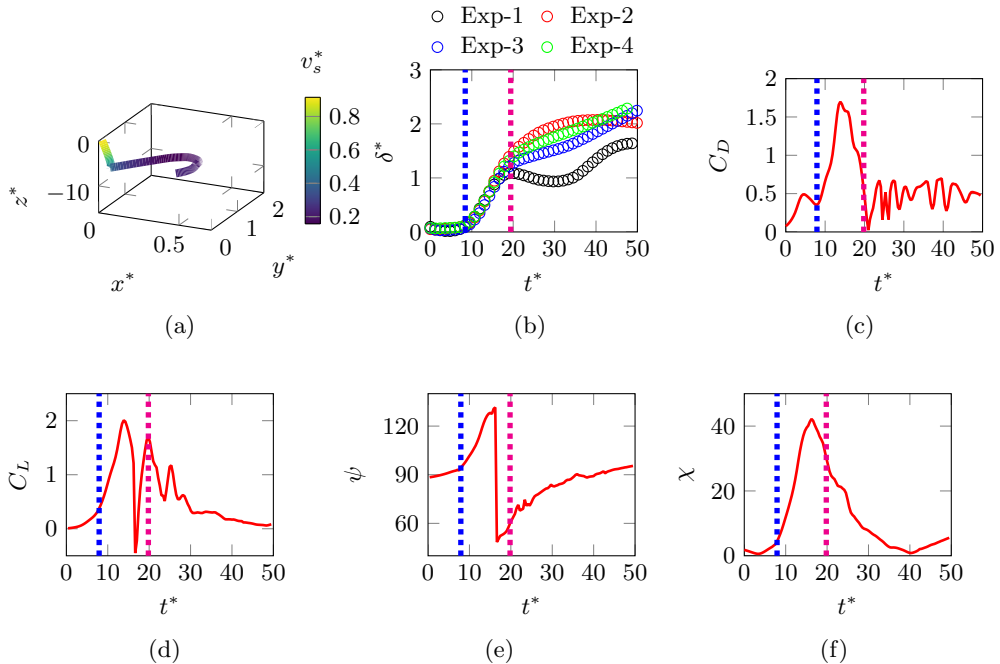


Figure 8: Penetration of a 10 mm sphere of density ratio  $\rho^* = 2.16$  at  $Re_i = 22300$ . (a) Three-dimensional rendition of pathline in dimensionless time; (b) Dimensionless lateral distance  $\delta^*$  for four repetitions of the same experiment; (c) Drag coefficient as a function of dimensionless time. (d) Lift coefficient as a function of dimensionless time. (e) and (f) represent angle  $\psi$  and angle  $\chi$  as a function of dimensionless time, respectively. The graphs (c)-(f) correspond to the red curve shown in graph (b). The color bar depicted in (a) illustrates the variation in dimensionless velocity ( $v_s^*$ ) of the sphere. The time step between the two successive points plotted in (b) is 6 ms.

effects since these would result in a skewed base pressure area on the rear of the sphere. Assuming the wall shear stress contributes little to the overall drag or lift, the integrated pressure over the sphere with a skewed wake would result in a drag and lift that would no longer be aligned with the motion axis of the sphere.

Whereas the drag coefficient rises to a maximum value and then decreases again towards the end of the deceleration phase (Fig. 8(c)), the lift coefficient exhibits strong fluctuations (Fig. 8(d)). This is very typical of all other data sets and can be explained by examining changes in the angle  $\psi$ . As discussed in subsection 2.4, when the trajectory goes through a 'projected' inflection point, this angle can exhibit sharp jumps in magnitude, since the orientation of curvature, i.e.,  $\mathbf{n}_\sigma$ , will change direction. Such a change is seen in Fig. 8(e), corresponding to a sharp drop in lift coefficient. We conclude that this arises due to a reorientation of the wake, such that the asymmetry changes orientation on the sphere. During this change, the wake is momentarily symmetric, leading to a short period of zero hydrodynamic lift. However, whereas the wake *orientation* is changing, the wake *area* apparently remains larger, resulting in a persistently larger drag coefficient, i.e., the wake base pressure still acts over an area undiminished in magnitude. Once through the point of changing  $\mathbf{n}_\sigma$ , the lift force is again high and in the direction of the new unit vector  $-\mathbf{n}_\sigma$ , i.e. positive.

What is further noteworthy in the deceleration phase is that the lateral deviation

$\delta^*$  exhibits a non-zero slope over longer periods, almost identical in all repetitions. As discussed above, this infers that a constant hydrodynamic lift in magnitude is sustained. In this case, the hydrodynamic lift counteracts the ever-present body forces (gravity and buoyancy), which are now contributing to the lift, since the sphere is no longer moving along a strictly vertical trajectory. With this balance between hydrodynamic lift and body force-induced lift, the sphere trajectory would turn vertical downward.

Phenomenologically, these observations are in excellent agreement with experiments from Truscott *et al.* (2012), where also all hydrophilic spheres exhibited a sharp deviation from the vertical followed by a rapid deceleration. Similarly, they attribute the sudden trajectory change to asymmetrical vortex shedding, as observed also by Horowitz & Williamson (2010). The direction of trajectory change was non-repeatable and depended on the direction of the shed vortex causing the trajectory deviation, as in the present experiments.

The deceleration phase ends where the absolute velocity magnitude reaches a minimum and again, this occurs for all investigated cases at a rather constant value of  $t^* \approx 20 - 21$ , as seen in Fig. 7. Typically, this minimum velocity is close to and sometimes slightly less than the terminal velocity, given in Eq. (2.4). For instance, in Fig. 4 for the 10 mm sphere, a slight acceleration is seen following the deceleration phase. This is likely due to a relaxation of the asymmetric wake into a symmetric, steady state condition, which is then maintained throughout the final settling phase. Note that Truscott *et al.* (2012) also observe for lighter spheres a velocity slightly less than the terminal velocity, followed by a light acceleration (their Fig. 5). They call this ‘underdamped behaviour’, but do not elaborate on its physical origins.

However, it is curious to observe that, despite the widely varying trajectories observed for repetitive experiments, the deceleration phase lasts over an extremely uniform dimensionless time of  $t^* \approx 20 - 21$  for all impact conditions. Assuming the end of the deceleration phase corresponds to conditions at which inertia no longer contributes significantly to the force balance (Eq. 2.3), it can be concluded that the time to dissipate the initial kinetic energy scales remarkably well with  $D/U$ , independent of impact Reynolds number and density ratio. Retrospectively, this is not surprising, since no other length or velocities scales are involved in the problem.

It is noteworthy that both the drag and lift coefficients attain rather high values during the deceleration phase. This is summarized in Fig. 9, in which the maximum attained drag coefficient in the deceleration phase is shown as a function of when it occurs (dimensionless time), at what velocity it occurs, and at what values of dimensionless acceleration it occurs (acceleration is dimensionless after differentiating the dimensionless velocity magnitude). There are several distinct trends observable in this data. For one, the maximum drag occurs within a narrow band of dimensionless time, all within the deceleration phase (Fig. 9(a)). A light trend toward higher dimensionless times for higher impact Reynolds numbers appears to be significant. Second, with a higher impact Reynolds number a sphere of constant diameter will experience a higher drag coefficient at lower dimensionless velocities (Fig. 9(b)) and lower dimensionless accelerations (Fig. 9(c)). Third, higher maximum drag coefficients correlate closely with lower dimensionless deceleration values (Fig. 9(c)). Fourth, these trends are similar for spheres of different density ratios, albeit the higher density ratio exhibits lower overall values of the maximum drag coefficient. To put these numerical values of velocity and acceleration into perspective, one might refer back to Fig. 4(c), which indicates that the dimensionless velocity approaches approx. 0.2 (0.1 - 0.2 is typical for all cases) and the dimensionless acceleration approaches values of zero (or even slightly positive) at the end of the deceleration phase (slope of the velocity curve in Fig. 4(c)). Finally, since all of

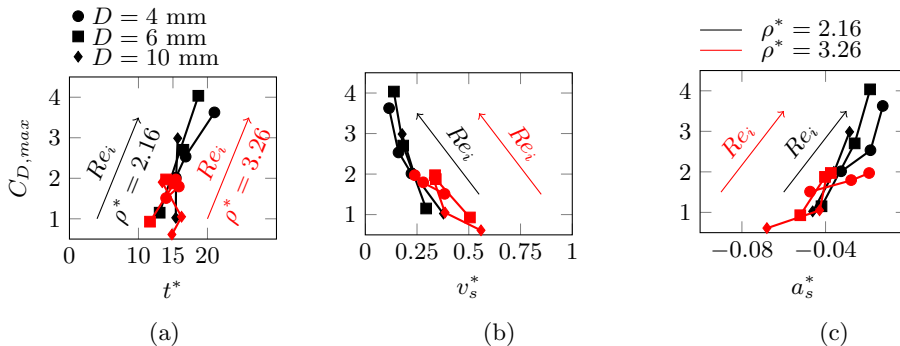


Figure 9: Analysis of maximum drag coefficients measured for various sphere diameters and density ratios (a) Dimensionless time of occurrence of maximum drag coefficient; (b) Dimensionless velocity at which maximum drag occurs; (c) Dimensionless acceleration at which maximum drag occurs. The arrow indicates the increase in  $Re_i$  of the sphere through a higher impact velocity.

the three graphs in Fig. 9 contain the same data points, it is evident that spheres moving with higher velocity experience also higher deceleration, which is to be expected since the drag force is proportional to the square of the velocity.

To interpret the above results, we now consider the flow around the sphere under conditions of strong acceleration/deceleration, particularly the behaviour of the boundary layer near its separation point. To observe the flow patterns around the sphere, a uniform coating of red dye was applied to the sphere before it was released into the quiescent liquid with a  $Re_i$  of 15700. Figure. 10a shows the resulting flow visualization around the sphere. The pressure distribution around the sphere is influenced by the asymmetric separation points in the wake region. For the Reynolds numbers encountered in this study, the boundary layer is expected to remain laminar up to separation. Under steady onflow conditions (which is not the case in the deceleration phase), separation would be expected near an angle of  $80^\circ$ - $84^\circ$ . The expected velocity profile of the boundary layer in the vicinity of separation is shown schematically in Fig. 10c, whereby the solid lines represent the boundary layer velocity profile at some instant in time. If the sphere experiences a strong acceleration, the outer flow would effectively increase in velocity, and over a short period of time, the separation point would move rearward, decreasing the wake area. This is indicated in the figure with a dashed line marked ‘accelerating sphere’. With a deceleration of the sphere, the opposite trend would be expected, i.e., the separation would occur earlier, resulting in a larger wake area over which the base pressure would be exerted. In the figure, this is indicated with the dashed velocity profile labelled ‘decelerating sphere’. This would result in a higher drag, consistent with the observations of the present study throughout the deceleration phase.

It is apparent from this data (Fig. 9), that the drag coefficient of a decelerating sphere at some instantaneous Reynolds number can be significantly higher than for a sphere experiencing a steady onflow at the same Reynolds number. Although there exist numerous studies of sphere drag under decelerating conditions, most of these are devoted to low Reynolds number flows (Liu *et al.* 2018; Velazquez & Barrero-Gil 2024; Temkin & Mehta 1982). Some studies of decelerating bluff bodies at similar Reynolds numbers have indicated that the drag coefficient can differ significantly from values for steady flow (Potvin *et al.* 2003), while others remain rather inconclusive about how drag changes for decelerating bodies (Marchildon & Gauvin 1979). Thus, at present it is



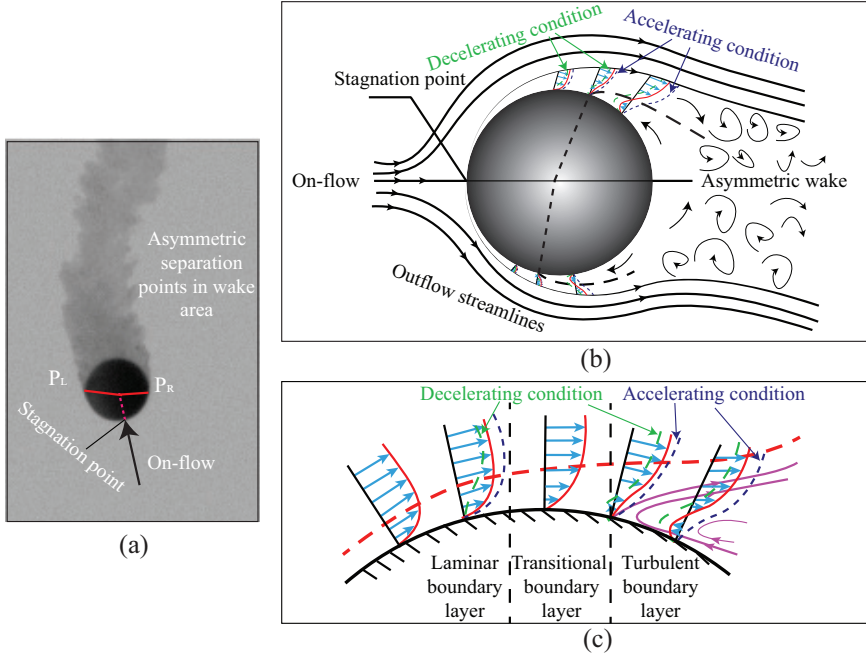


Figure 10: Schematic interpretation of the origins of lift and drag through wake asymmetry. (a) Visualization of a free-falling sphere ( $\rho^* = 2.16$ ,  $D = 10$  mm and  $Re_i = 15700$ ), showing a change in trajectory and indicating an asymmetry of the left ( $P_L$ ) and right ( $P_R$ ) points of separation. (b) Schematic (and exaggerated) visualization of asymmetric wake area arising from asymmetric separation points, indicating that relative to the on-flow, a lift force component arises. (c) Schematic (and exaggerated) interpretation of how a deceleration or acceleration of the sphere might influence the boundary-layer velocity profile in the vicinity of a separation point.

difficult to find corroborating data to our experimental results.

Similarly, little quantitative literature exists on unsteady lift forces in this Reynolds number range, as confirmed in the exhaustive survey of spherical particles in unbounded flows given by Shi & Rzehak (2019). Nevertheless, it is clear that bifurcations and symmetry breaking in the wake of spheres occur already at relatively low Reynolds numbers and result in a random change of direction (Fabre *et al.* 2008). The magnitude of these lift forces in the present Reynolds number range has, to the authors' knowledge, not been previously measured.

This transient state of the boundary layer during sphere deceleration is analogous to Stokes first problem in which the similarity variable  $\eta = y/2\sqrt{\nu t}$  is used to describe the invoked velocity profile above a plate, suddenly accelerated to some finite velocity (Spurk & Aksel 2007). Interpreting  $y$  as the boundary-layer thickness in the present case, the time necessary for the diffusion of a strong change of outer flow velocity into the same dimensionless state near the sphere surface would scale with  $y^2$ . If, for instance, one boundary layer was only half as thick as a second boundary layer, a change of outer velocity would be felt in  $0.5^2 = 0.25$  the time. Given that the boundary-layer thickness over the sphere will scale approximately with  $Re^{1/2}$ , the spheres with higher impact Reynolds numbers would exhibit a lower boundary-layer thickness. Hence, this should lead to an earlier and stronger influence on the separation point, resulting in a higher

drag. This is consistently seen in the data of Fig. 9.

The spheres with a higher density ratio will have higher inertial forces for the same Reynolds number; hence, any wake variations will have a relatively lower effect on the overall sphere motion, resulting in less modulation of the computed drag coefficient using Eq. (2.3). The results shown in Fig. 9 confirm that spheres with higher density ratios exhibit lower maximum drag coefficients.

#### *Settling phase*

The settling phase is prominently characterised with widely varying values of lateral deviation  $\delta^*$ , as shown in Fig. 5, but also evident in Fig. 8(b). During this phase, the velocity is very low, and inertia no longer plays a dominant role. Thus, the trajectory is now highly susceptible to even small lift forces arising from wake asymmetries. Thus, the trajectory curvatures become more frequent and pronounced. This leads to variations in drag coefficient, but now only seen as smaller variations near values typical of steady-state flow, i.e.,  $C_D \approx 0.5$ . Similarly, the lift coefficient reduces in magnitude, approaching values near zero. These variations, both in drag and lift, are still attributed to a fluctuating and non-symmetric wake structure, but its consequence is now much less significant.

If observed long enough, one would expect the angle  $\chi$ , which is the angle subtending the trajectory direction and the gravity vector, to approach zero. This is observed in many of our experiments, but not in all, e.g., Fig. 8e. In these cases, the field and/or observation time was insufficient for this condition to set in. Nonetheless, in all of the experiments, the sphere velocity approached the terminal velocity, as computed using Eq. (2.4).

## 4. Conclusions

This study has examined the trajectories of free-falling spheres penetrating a deep pool, subjected to self-excited variations of lift and drag forces. The origins of these forces are attributed to unsteady and asymmetric wake behavior, whereby the magnitude of the forces has been evaluated using a complete force balance given by the BBO equation formulated in a natural coordinate system. Extremely consistent behaviour has been observed over a large range of impact Reynolds numbers and density ratios, classified into three phases, denoted the submersion, decelerating, and settling phases, respectively. Several novel conclusions can be summarized from this work. For one, the three distinct phases occur over virtual identical dimensionless time periods, indicating a universal scaling with  $U/D$  over the entire examined parameter range. A second observation is that the spheres in a deceleration state can exhibit drag coefficients far exceeding those found for steady on-flow conditions. These drag forces are inseparable from accompanying lift forces, which themselves are responsible for variations in trajectory direction. Understandably, with decreasing velocity (and inertial forces), the trajectories become more susceptible to the fluctuating forces arising from the unsteady wake behavior.

Several questions remain unanswered from this study. For one, it is apparent that in the settling phase, the lift force often compensates the body forces (gravity and buoyancy) in such a manner, that the lateral deviation grows at a constant rate. This stability of the lift force in both direction and magnitude over considerable path lengths suggests that the randomness observed in the initial directional deviation of the sphere from its vertical trajectory is no longer present. We have no clear explanation for this observed phenomenon.

Despite the understanding that this study has brought to the subject, many explanations

remain speculative in the sense that the boundary separation and postulated unsteady changes in the wake area and orientation were not directly measured. Measuring or computing the boundary layer on a free-falling body in three dimensions around the sphere, and with sufficient resolution to resolve separation, will be a challenge, but could contribute to a more complete understanding of this unsteady flow behavior.

## Acknowledgement

The author C. Tropea acknowledges support from the Indian Institute of Technology Madras through the appointment as the Henry Ford Chair Professor in Mechanical Engineering.

## Declaration of interests

The authors report no conflict of interest.

## REFERENCES

- ABRAHAM, JOHN, GORMAN, JOHN, RESEGHETTI, FRANCO, SPARROW, EPHRAIM, STARK, JOHN & SHEPARD, THOMAS 2014 Modeling and numerical simulation of the forces acting on a sphere during early-water entry. *Ocean Engineering* **76**, 1–9.
- ACHENBACH, ELMAR 1974 Vortex shedding from spheres. *Journal of Fluid Mechanics* **62** (2), 209–221.
- AFFELD, K, SCHICHL, K & ZIEMANN, A 1993 Assessment of rowing efficiency. *International Journal of Sports Medicine* **14** (S 1), S39–S41.
- ARISTOFF, JEFFREY M. & BUSH, JOHN W.M. 2009 Water entry of small hydrophobic spheres. *Journal of Fluid Mechanics* **619**, 45–78.
- ARISTOFF, JEFFREY M., TRUSCOTT, TADD T., TECHET, ALEXANDRA H. & BUSH, JOHN W.M. 2010 The water entry of decelerating spheres. *Physics of Fluids* **22** (3), 1–8.
- BARLOW, JEWEL B & DOMANSKI, MICHAEL J 2008 Lift on stationary and rotating spheres under varying flow and surface conditions. *AIAA Journal* **46** (8), 1932–1936.
- BILLA, PRASANNA KUMAR, JOSYULA, TEJASWI, TROPEA, CAMERON & MAHAPATRA, PALLAB SINHA 2024 Supplementary material to the publication Motion of a rigid sphere entering and penetrating a deep pool. *DOI and URL to be added after acceptance* .
- CHRISTIANSEN, EB & BARKER, DEE H 1965 The effect of shape and density on the free settling of particles at high Reynolds numbers. *AIChE Journal* **11** (1), 145–151.
- CONSTANTINESCU, GEORGE & SQUIRES, KYLE 2004 Numerical investigations of flow over a sphere in the subcritical and supercritical regimes. *Physics of Fluids* **16** (5), 1449–1466.
- CROWE, CLAYTON T, SCHWARZKOPF, JOHN D, SOMMERFELD, MARTIN & TSUJI, YUTAKA 2011 *Multiphase flows with droplets and particles*. CRC Press LLC Boca Raton, FL.
- DUCLAUX, V., CAILLÉ, F., DUEZ, C., YBERT, C., BOCQUET, L. & CLANET, C. 2007 Dynamics of transient cavities. *Journal of Fluid Mechanics* **591**, 1–19.
- ERN, PATRICIA, RISSO, FRÉDÉRIC, FABRE, DAVID & MAGNAUDET, JACQUES 2011 Wake-induced oscillatory paths of bodies freely rising or falling in fluids. *Annual Review of Fluid Mechanics* **44**, 97–121.
- FABRE, DAVID, AUGUSTE, FRANCK & MAGNAUDET, JACQUES 2008 Bifurcations and symmetry breaking in the wake of axisymmetric bodies. *Physics of Fluids* **20** (5).
- FAGE, ARTHUR 1936 Experiments on a sphere at critical Reynolds numbers. *Aero. Res. Council Gt. Brit.* .
- FALTINSEN, O 1990 Sea loads on ships and offshore structures. *The Press Syndicate of the University of Cambridge* .
- GREGORIO, ELIZABETH, BALARAS, ELIAS & LEFTWICH, MEGAN C 2023 Air cavity deformation by single jointed diver model entry bodies. *Experiments in Fluids* **64**, 168.

- GUO, JUNKE 2011 Motion of spheres falling through fluids. *Journal of Hydraulic Research* **49** (1), 32–41.
- HADŽIĆ, I, BAKIĆ, V, PERIĆ, M, ŠAJN, V & KOSEL, F 2002 Experimental and numerical studies of flow around sphere at sub-critical Reynolds number. In *Engineering Turbulence Modelling and Experiments 5*, pp. 667–676. Elsevier.
- HOROWITZ, M & WILLIAMSON, CHK 2010 The effect of Reynolds number on the dynamics and wakes of freely rising and falling spheres. *Journal of Fluid Mechanics* **651**, 251–294.
- HOWISON, SD, OCKENDON, JR & OLIVER, JM 2002 Deep-and shallow-water slamming at small and zero deadrise angles. *Journal of Engineering Mathematics* **42**, 373–388.
- HOWISON, SD, OCKENDON, JR & WILSON, SK 1991 Incompressible water-entry problems at small deadrise angles. *Journal of Fluid Mechanics* **222**, 215–230.
- KAYS, WILLIAM MORROW, CRAWFORD, MICHAEL E & WEIGAND, BERNHARD 1980 *Convective Heat and Mass Transfer*, , vol. 4. McGraw-Hill, New York.
- KOROBKIN, A. 1988 Initial Stage Of Water Impact. *Annual Review of Fluid Mechanics* **20** (1), 159–185.
- KOVASZNAV, LSG, TANI, ITIRO, JKAWAMURA, M & FUJITA, HAJIME 1971 Instantaneous pressure distribution around a sphere in unsteady flow. *Tech. Rep.*. ONR No. 00014-67.0163-002, The John Hopkins University.
- KUWABARA, GORO, CHIBA, SEIJI & KONO, KIMITOSHI 1983 Anomalous motion of a sphere falling through water. *Journal of the Physical Society of Japan* **52** (10), 3373–3381.
- LIU, FANGLIN, LIU, PEIQING, QU, QIULIN, LIN, LI, HU, TIANXIANG & AGARWAL, RAMESH K 2018 Numerical study of flow physics and drag of spheres in unsteady motion. In *2018 Fluid Dynamics Conference*, p. 3082.
- MANSOOR, M. M., MARSTON, J. O., VAKARELSKI, I. U. & THORODDSEN, S. T. 2014 Water entry without surface seal: Extended cavity formation. *Journal of Fluid Mechanics* **743**, 295–326.
- MANSOOR, M. M., VAKARELSKI, I. U., MARSTON, J. O., TRUSCOTT, T. T. & THORODDSEN, S. T. 2017 Stable-streamlined and helical cavities following the impact of Leidenfrost spheres. *Journal of Fluid Mechanics* **823**, 716–754.
- MARCHILDON, EK & GAUVIN, WH 1979 Effects of acceleration, deceleration and particle shape on single-particle drag coefficients in still air. *AIChE Journal* **25** (6), 938–948.
- MAY, ALBERT 1951 Effect of surface condition of a sphere on its water-entry cavity. *Journal of Applied Physics* **22** (10), 1219–1222.
- MAY, ALBERT 1975 *Water entry and the cavity-running behavior of missiles*. US Government Printing Office.
- MCMALE, GLEN, SHIRTCLIFFE, NJ, EVANS, CR & NEWTON, MI 2009 Terminal velocity and drag reduction measurements on superhydrophobic spheres. *Applied Physics Letters* **94** (6), 064104.
- MEHTA, RAKHAB C 2023 Aerodynamics of sport balls, badminton shuttlecock and javelin. *Sch J Eng Tech* **2**, 4–16.
- NORMAN, AK & MCKEON, BJ 2011 The effect of a small isolated roughness element on the forces on a sphere in uniform flow. *Experiments in Fluids* **51** (4), 1031–1045.
- NOURI, R., GANJI, D. D. & HATAMI, M. 2014 Unsteady sedimentation analysis of spherical particles in Newtonian fluid media using analytical methods. *Propulsion and Power Research* **3** (2), 96–105.
- PALLIS, JM & MEHTA, RD 2002 Aerodynamics and hydrodynamics in sports. *The Engineering of Sport* **4**, 31–39.
- POTVIN, J, PEEK, G & BROCATO, B 2003 New model of decelerating bluff-body drag. *Journal of Aircraft* **40** (2), 370–377.
- RICHARDSON, EG 1948 The impact of a solid on a liquid surface. *Proceedings of the Physical Society* **61** (4), 352.
- RUBINOW, S. I. & KELLER, JOSEPH B. 1961a The transverse force on a spinning sphere moving in a viscous fluid. *Journal of Fluid Mechanics* **11** (3), 447–459.
- RUBINOW, SOL I & KELLER, JOSEPH B 1961b The transverse force on a spinning sphere moving in a viscous fluid. *Journal of Fluid Mechanics* **11** (3), 447–459.
- SAFFMAN, PHILIP GEOFFREY 1965 The lift on a small sphere in a slow shear flow. *Journal of Fluid Mechanics* **22** (2), 385–400.

- SAKIB, NAZMUS & SMITH, BARTON L 2020 Study of the reverse Magnus effect on a golf ball and a smooth ball moving through still air. *Experiments in Fluids* **61**, 1–9.
- SCOGGINS, JAMES R 1967 *Sphere behavior and the measurement of wind profiles*. National Aeronautics and Space Administration.
- SHAFRIR, URI 1965 *Horizontal oscillations of falling spheres*. University of California, Los Angeles, Institute of Geophysics and Planetary Science.
- SHI, PENGYU & RZEHA, ROLAND 2019 Lift forces on solid spherical particles in unbounded flows. *Chemical Engineering Science* **208**, 115145.
- SPURK, JOSEPH & AKSEL, NURI 2007 *Fluid Mechanics*. Springer Science & Business Media.
- STOKES, GEORGE GABRIEL & OTHERS 1851 On the effect of the internal friction of fluids on the motion of pendulums .
- TAN, BENEDICT C.W., VLASKAMP, J. H.A., DENISSENKO, P. & THOMAS, P. J. 2016 Cavity formation in the wake of falling spheres submerging into a stratified two-layer system of immiscible liquids. *Journal of Fluid Mechanics* **790**, 33–56.
- TANEDA, SADATOSHI 1978 Visual observations of the flow past a sphere at Reynolds numbers between  $10^4$  and  $10^6$ . *Journal of Fluid Mechanics* **85** (1), 187–192.
- TECHET, A. H. & TRUSCOTT, T. T. 2011 Water entry of spinning hydrophobic and hydrophilic spheres. *Journal of Fluids and Structures* **27** (5–6), 716–726.
- TEMKIN, S & MEHTA, HK 1982 Droplet drag in an accelerating and decelerating flow. *Journal of Fluid Mechanics* **116**, 297–313.
- TRUSCOTT, TADD T., EPPS, BRENDEN P. & BELDEN, JESSE 2014 Water entry of projectiles. *Annual Review of Fluid Mechanics* **46**, 355–378.
- TRUSCOTT, TADD T, EPPS, BRENDEN P & TECHET, ALEXANDRA H 2012 Unsteady forces on spheres during free-surface water entry. *Journal of Fluid Mechanics* **704**, 173–210.
- TRUSCOTT, TADD T. & TECHET, ALEXANDRA H. 2009 A spin on cavity formation during water entry of hydrophobic and hydrophilic spheres. *Physics of Fluids* **21** (12), 1–4.
- VAKARELSKI, IVAN U., KLASEBOER, EVERT, JETLY, ADITYA, MANSOOR, MOHAMMAD M., AGUIRRE-PABLO, ANDRES A., CHAN, DEREK Y.C. & THORODDSEN, SIGURDUR T. 2017 Self-determined shapes and velocities of giant near-zero drag gas cavities. *Science Advances* **3** (9), 1–8.
- VAKARELSKI, IVAN U., MARSTON, JEREMY O., CHAN, DEREK Y.C. & THORODDSEN, SIGURDUR T. 2011 Drag reduction by leidenfrost vapor layers. *Physical Review Letters* **106** (21), 3–6.
- VALLADARES, R. M., GOLDSTEIN, P., STERN, C. & CALLES, A. 2003 Simulation of the motion of a sphere through a viscous fluid. *Revista Mexicana de Fisica* **49** (2), 166–174.
- VELAZQUEZ, A & BARRERO-GIL, A 2024 Simplified dynamics model of a sphere decelerating freely in a fluid. *Physics of Fluids* **36** (2).
- VELDHUIS, CHRISTIAN, BIESHEUVEL, ARIE, VAN WIJNGAARDEN, LEEN & LOHSE, DETLEF 2005 Motion and wake structure of spherical particles. *Nonlinearity* **18** (1).
- VON KARMAN, TH. 1929 The impact on seaplane floats during landing. *National Advisory Committee on Aeronautics* .
- WORTHINGTON, ARTHUR MASON 1883 On impact with a liquid surface. *Proceedings of the Royal Society of London* **34** (220–223), 217–230.
- YUN, GIWOONG, KIM, DONGJOO & CHOI, HAECHEON 2006 Vortical structures behind a sphere at subcritical Reynolds numbers. *Physics of Fluids* **18** (1).
- ZHAO, RONG & FALTINSEN, ODD 1993 Water entry of two-dimensional bodies. *Journal of Fluid Mechanics* **246**, 593–612.
- ZHU, C & FAN, LS 1998 Multiphase flow: Gas/solid. In *The Handbook of Fluid Dynamics*. CRC Press LLC Boca Raton, FL.